MoP3SiO11: A 4d3 honeycomb antiferromagnet with disconnected octahedra

Danis I Badrtdinov, Lei Ding, Clemens Ritter, Jan Hembacher, Niyaz Ahmed, Yurii Skourski, Alexander A Tsirlin

Editors' Suggestion

MoP_3SiO_{11}: A $4d^3$ honeycomb antiferromagnet with disconnected octahedra

Danis I. Badrtdinov,[1] Lei Ding,[2,3] Clemens Ritter,[4] Jan Hembacher,[5] Niyaz Ahmed,[5,6] Yurii Skourski,[7] and Alexander A. Tsirlin[5,1,*]

[1]*Theoretical Physics and Applied Mathematics Department, Ural Federal University, 620002 Yekaterinburg, Russia*
[2]*ISIS Facility, Rutherford Appleton Laboratory, Harwell Oxford, Didcot, United Kingdom*
[3]*Institut Néel, CNRS and Université Joseph Fourier, 38042 Grenoble, France*
[4]*Institut Laue-Langevin, BP 156, F-38042 Grenoble, France*
[5]*Experimental Physics VI, Center for Electronic Correlations and Magnetism, Institute of Physics, University of Augsburg, 86135 Augsburg, Germany*
[6]*School of Physics, Indian Institute of Science Education and Research, Thiruvananthapuram-695551, India*
[7]*Dresden High Magnetic Field Laboratory (HLD-EMFL), Helmholtz-Zentrum Dresden-Rossendorf, 01328 Dresden, Germany*

(Received 18 July 2021; accepted 8 September 2021; published 22 September 2021)

We report the crystal structure and magnetic behavior of the $4d^3$ spin-3/2 silicophosphate MoP_3SiO_{11} studied by high-resolution synchrotron x-ray diffraction, neutron diffraction, thermodynamic measurements, and *ab initio* band-structure calculations. Our data revise the crystallographic symmetry of this compound and establish its rhombohedral space group ($R\bar{3}c$) along with the geometrically perfect honeycomb lattice of the Mo^{3+} ions residing in disconnected MoO_6 octahedra. Long-range antiferromagnetic order with the propagation vector $\mathbf{k} = 0$ observed below $T_N = 6.8$ K is a combined effect of the nearest-neighbor in-plane exchange coupling $J \simeq 2.6$ K, easy-plane single-ion anisotropy $D \simeq 2.2$ K, and a weak interlayer coupling $J_c \simeq 0.8$ K. The 12% reduction in the ordered magnetic moment of the Mo^{3+} ions and the magnon gap of $\Delta \simeq 7$ K induced by the single-ion anisotropy further illustrate the impact of spin-orbit coupling on the magnetism. Our analysis puts forward single-ion anisotropy as an important ingredient of $4d^3$ honeycomb antiferromagnets despite their nominally quenched orbital moment.

DOI: 10.1103/PhysRevB.104.094428

I. INTRODUCTION

The honeycomb interaction geometry takes a special place in the physics of magnetic insulators. The bipartite nature of the honeycomb lattice excludes geometrical frustration for nearest-neighbor interactions [1,2], but allows interesting cases of exchange frustration in the presence of strong spin-orbit coupling when Kitaev and off-diagonal anisotropic terms become dominant interactions [3,4]. Experimental observations of Kitaev magnetism in $4d^5$ and $5d^5$ compounds with the effective spin 1/2 [5], such as α-$RuCl_3$ [6] and different polymorphs of Li_2IrO_3 [7], have triggered a broader interest in honeycomb magnets. On the theory side, proposals of Kitaev physics beyond the effective spin 1/2 have been put forward [8], with implications for spin-orbit-coupled d^4 magnetic ions represented by Ru^{4+} [9,10].

Compared to d^5 and d^4, the $4d^3$ case of Ru^{5+} may seem less exotic, because the half-filling of the t_{2g} shell quenches the orbital moment. Nevertheless, the Affleck-Kennedy-Lieb-Tasaki (AKLT) phase, a model entangled state for quantum computation [12], was predicted to appear in d^3 systems in the limit of weak Hund's coupling J_H [13,14]. On increasing J_H, this AKLT phase transforms into a Néel-ordered state that has been observed experimentally in $SrRu_2O_6$ [15] and caused significant attention because of its very high Néel temperature of 565 K and an unusually low ordered moment of only 1.3–1.4 μ_B [16,17] compared to 3 μ_B expected for a spin-3/2 ion. These observations could not be explained on the level of a simple nearest-neighbor Heisenberg Hamiltonian. An unusual electronic state with hexagon molecular orbitals was proposed [18] and subsequently investigated theoretically and experimentally [19–22], although a more conventional description on the level of a Heisenberg Hamiltonian with an additional single-ion anisotropy term [23] proved sufficient for explaining magnetic excitations of this material [24]. The isoelectronic compound $AgRuO_3$ shows a similar phenomenology, albeit with a somewhat lower T_N of 342 K [25,26].

Beyond ruthenates, several recent studies discussed the possibility of Kitaev interactions and other anisotropic exchange interactions in spin-3/2 honeycomb ferromagnets, such as CrI_3 [27–31]. This raises the question whether the on-site (single-ion) anisotropy or different inter-site effects (Kitaev anisotropy, hexagon molecular orbitals) should be used to describe magnetism of the d^3 honeycomb systems. To address this question, we consider MoP_3SiO_{11} silicophosphate [32], the $4d^3$ honeycomb antiferromagnet with disconnected transition-metal octahedra (Fig. 1). Increased separations between the magnetic ions suppress intersite effects and expose single-ion anisotropy as the dominant anisotropy term despite the nominally quenched orbital moment.

*altsirlin@gmail.com

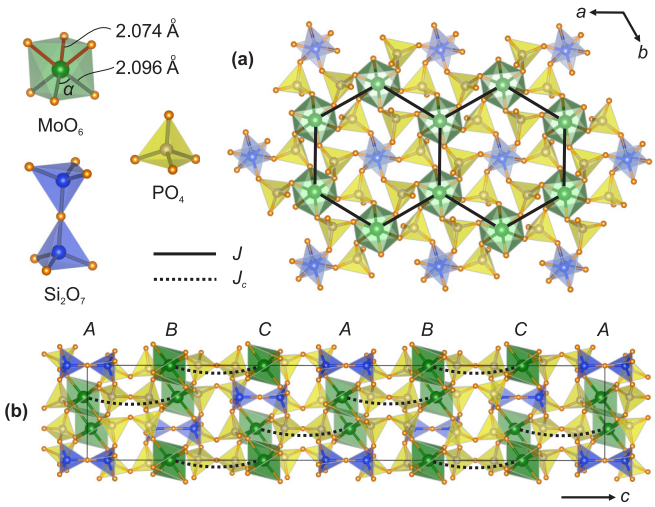

FIG. 1. Rhombohedral crystal structure of MoP_3SiO_{11}: (a) honeycomb planes of the MoO_6 octahedra separated by the PO_4 tetrahedra; the Si_2O_7 units center the hexagons; (b) *ABCABC* stacking of the honeycomb planes and the interlayer couplings J_c through the shortest Mo–Mo contacts between the planes. VESTA software was used for crystal structure visualization [11].

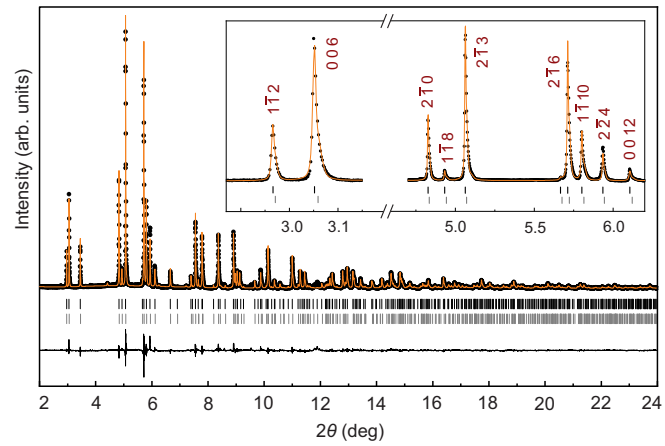

FIG. 2. Rietveld refinement for the room-temperature high-resolution XRD data collected on the phase-pure sample of MoP_3SiO_{11}. The refined model included two $R\bar{3}c$ phases with the slightly different c lattice parameters [$c_1 = 39.9085(5)$ Å, $c_2 = 39.812(2)$ Å]. The inset shows the asymmetric peak broadening, which is more pronounced in the hkl reflections with large l. The refinement residuals are $R_I = 0.045$ and $R_p = 0.072$.

II. METHODS

Polycrystalline samples of MoP_3SiO_{11} were prepared by a two-step solid-state reaction. First, a mixture of MoO_3, SiO_2, and $(NH_4)_2HPO_4$ taken in the 0.5:1:3 molar ratio was annealed in air at 600 °C for 24 hours. The reaction produced a dark-green melted product that was re-ground, mixed with Mo powder (Alfa Aesar, 2–4 micron particle size) according to the MoP_3SiO_{11} stoichiometry, and annealed at 870 °C for 100 hours. This second annealing was performed in a sealed quartz tube filled with 300 mbar of argon to prevent oxidation of Mo^{3+}. The brownish-green product was phase-pure MoP_3SiO_{11} when smaller samples with the total mass of 0.1–0.2 g were prepared. For larger samples, minor amounts of the MoP_2O_7 impurity were observed.

High-resolution x-ray diffraction (XRD) data [33] were collected at room temperature at the ID22 beamline of the European Synchrotron Radiation Facility (ESRF), Grenoble using the wavelength of 0.35424 Å. The sample was loaded into a thin borosilicate glass capillary and spun during the measurement. The diffracted signal was measured by 9 scintillation detectors, each preceded by a Si (111) analyzer crystal.

Neutron diffraction data [34] were collected at the D2B ($\lambda = 1.594$ Å) and D20 ($\lambda = 2.41$ Å) instruments at the Institut Laue-Langevin (ILL), Grenoble. The powder sample of MoP_3SiO_{11} was loaded into a vanadium container and cooled down to 1.5 K with the standard Orange cryostat. Rietveld refinements were performed in JANA2006 [35] and FULLPROF [36].

Temperature-dependent magnetic susceptibility was measured with MPMS3 SQUID magnetometer from Quantum Design in the temperature range of 1.8–300 K in applied fields up to 7 T. Magnetization measurements up to 56 T were performed in Dresden High Magnetic Field Laboratory at 1.4 K on a powder sample loaded into a thin kapton tube. Heat capacity was measured in the temperature range of 1.8–300 K in magnetic fields up to 14 T on a pressed pellet by the relaxation method using Quantum Design PPMS.

Electronic structure calculations were performed on the level of density-functional theory (DFT) utilizing the generalized gradient approximation (GGA) [37]. To this end, QUANTUM ESPRESSO [38] and Vienna *ab initio* simulation package (VASP) [39,40] codes with the plane-wave basis set were used. The energy cutoff was set at 700 eV and the energy convergence criteria was 10^{-6} eV. For the Brillouin-zone integration, a 4×4×4 Monkhorst-Pack mesh was used.

Thermodynamic properties of the magnetic model parameterized by DFT were obtained from quantum Monte-Carlo (QMC) simulations performed using the LOOP [41] and DIRLOOP_SSE [42] algorithms of the ALPS simulation package [43]. We performed simulations on $L \times L \times L/2$ finite lattices with $L \leqslant 20$, where the unit cell contains eight magnetic sites with spin $S = 3/2$.

III. EXPERIMENTAL RESULTS

A. Crystal structure

The crystal structure of MoP_3SiO_{11} (Fig. 1) features honeycomb layers of the MoO_6 octahedra, which are separated by the PO_4 tetrahedra. This type of structural geometry is very different from the dense layers of transition-metal octahedra typically encountered in hexagonal magnets, such as α-Li_2IrO_3 and $SrRu_2O_6$. The increased nearest-neighbor Mo–Mo distance of 4.9 Å allows the hexagons to accommodate large Si_2O_7 pyrosilicate units in the center, whereas the PO_4 tetrahedra located above and below these hexagons condense into P_2O_7 units that connect adjacent layers stacked along the c axis.

Although monoclinic $C2/c$ symmetry has been reported for MoP_3SiO_{11} earlier [32], several structural parameters indicate that this crystal structure can be described as rhombohedral. Indeed, the b/a ratio of 1.7329(4) is very close to $\sqrt{3}$,

TABLE I. Atomic positions and atomic displacement parameters (U_{iso}, in 10^{-2} Å^2) for MoP_3SiO_{11} refined against the D2B data at 1.5 and 295 K. The lattice parameters are $a = 8.3952(3)$ Å, $c = 39.869(2)$ Å at 1.5 K and $a = 8.4015(3)$ Å, $c = 39.847(2)$ Å at 295 K. The space group is $R\bar{3}c$. The refinement residuals are $R_I = 0.025$, $R_p = 0.023$ at 1.5 K and $R_I = 0.033$, $R_p = 0.025$ at 295 K. The U_{iso} for oxygen atoms have been constrained. The cif-files are available as Ref. [45].

	Site		x/a	y/b	z/c	U_{iso}
Mo	12*c*	1.5 K	0	0	0.1592(1)	0.05(9)
		295 K	0	0	0.1593(1)	0.33(11)
P	36*f*	1.5 K	0.3712(4)	0.0331(4)	0.1193(1)	0.21(8)
		295 K	0.3702(5)	0.0323(5)	0.1190(1)	0.64(9)
Si	12*c*	1.5 K	0	0	0.4602(2)	0.9(2)
		295 K	0	0	0.4607(2)	0.9(2)
O1	36*f*	1.5 K	0.2868(4)	0.8178(4)	0.1132(1)	0.23(3)
		295 K	0.2879(5)	0.8180(5)	0.1134(1)	0.89(5)
O2	36*f*	1.5 K	0.2225(5)	0.0751(5)	0.1270(1)	0.23(5)
		295 K	0.2237(6)	0.0750(6)	0.1271(1)	0.89(5)
O3	36*f*	1.5 K	0.5279(4)	0.1025(4)	0.1435(1)	0.23(5)
		295 K	0.5282(5)	0.1048(5)	0.1434(1)	0.89(5)
O4	18*e*	1.5 K	0.7867(5)	0	$\frac{1}{4}$	0.23(5)
		295 K	0.7858(6)	0	$\frac{1}{4}$	0.89(5)
O5	6*a*	1.5 K	0	0	0	0.23(5)
		295 K	0	0	0	0.89(5)

whereas MoO_6 octahedra are three-fold symmetric. Moreover, the trigonal $R\bar{3}c$ symmetry was reported for a sister compound RuP_3SiO_{11} [44].

We used high-resolution XRD to verify the rhombohedral symmetry of MoP_3SiO_{11}. No peak splitting could be observed, and the data were successfully refined in the rhombohedral structure ($R\bar{3}c$). A closer inspection of the XRD pattern reveals that some of the peaks are asymmetrically broadened (Fig. 2), but this broadening is incompatible with the monoclinic distortion. For example, the broadening is observed for the 006 reflection that would not be split in $C2/c$. The asymmetry is most pronounced in the *hkl* reflections with large l and can be described by a second phase with the reduced lattice parameter c. This rather subtle broadening effect is not detectable using laboratory XRD and may be related to the stacking disorder. It does not affect any of the magnetic properties shown below.

Crystal structure refinements of the neutron diffraction data (Table I) were also performed in $R\bar{3}c$, but with only one phase because the asymmetric broadening was beyond the resolution of the D2B diffractometer. The refinement confirms the regular hexagonal arrangement of the Mo^{3+} ions located in trigonally distorted MoO_6 octahedra with the Mo–O distances of 2.074(5) and 2.096(7) Å, respectively. The stacking of the honeycomb planes follows the *ABCABC* sequence with six layers per unit cell [Fig. 1(b)]. No significant structural changes are observed upon cooling from room temperature to 1.5 K. The shortest interlayer Mo–Mo separation of 7.264 Å is much longer than that in other honeycomb magnets, such as $SrRu_2O_6$ (5.23 Å [15]) and CrI_3 (6.59 Å [46]).

B. Thermodynamic properties

Magnetic susceptibility of MoP_3SiO_{11} reveals the Curie-Weiss behavior at high temperatures, followed by a peak around 7 K (Fig. 3). Above 50 K, the fit with the modified Curie-Weiss law, $\chi(T) = \chi_0 + C/(T - \Theta)$, returns the temperature-independent contribution $\chi_0 = (3.0 \pm 0.1)\times10^{-5}$ emu/mol, Curie constant $C = 1.56 \pm 0.06$ emu K/mol, and Curie-Weiss temperature $\Theta = -10.7 \pm 0.4$ K. The Curie constant corresponds to the paramagnetic effective moment of 3.53 μ_B and $g = 1.82$ according to $\mu_{eff} = g\sqrt{S(S+1)}$ for $S = \frac{3}{2}$ of Mo^{3+}. The deviation from the free-electron value of $g \simeq 2.0$ gauges the effect of spin-orbit coupling on the single-ion physics. This effect is more pronounced than in $Mo(PO_3)_3$ with $g \simeq 1.93$ [47] ($C = 1.71$ emu K/mol) and especially in the Cr^{3+} compounds with $g \simeq 2.0$ [48,49]. On the other hand, an even larger reduction in the g-value has been reported for Mo^{4+} with $g = 1.6$–1.7 [50,51], because its $4d^2$ electronic configuration usually does not lead to quenching of the orbital moment.

The negative value of Θ indicates predominant antiferromagnetic couplings that are independently gauged by the

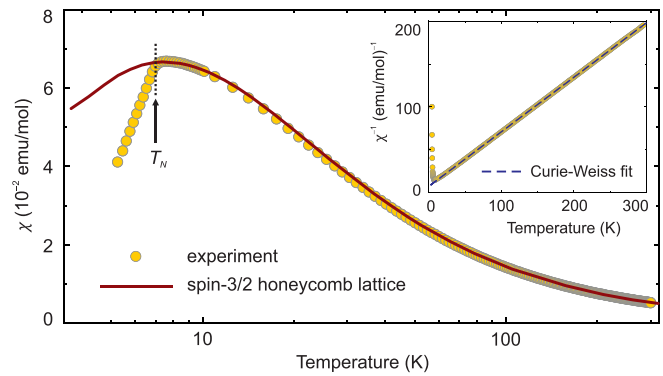

FIG. 3. Magnetic susceptibility (χ) of MoP_3SiO_{11} measured in the applied field of 0.01 T (circles) and the fit with the model of spin-3/2 honeycomb planes, $J = 2.6$ K (solid line). The inset shows inverse susceptibility and the Curie-Weiss fit.

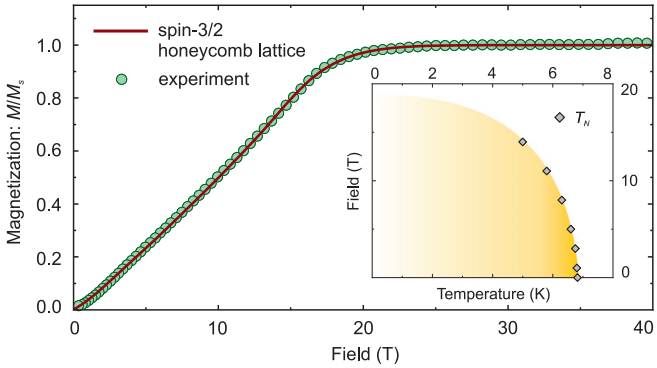

FIG. 4. Magnetization curve measured at 1.4 K in pulsed fields, with absolute values of M scaled to the saturated value M_s. The solid line is the fit with the model of spin-3/2 honeycomb planes, $J = 2.6$ K. The inset shows field-temperature phase diagram, with diamonds depicting the T_N values extracted from the specific-heat data (Fig. 5).

saturation field of about 18 T observed in the pulsed-field measurement (Fig. 4). The susceptibility peak at $T_N = 6.8$ K reflects long-range antiferromagnetic ordering. This transition also manifests itself by the sharp λ-type anomaly in the specific heat. The ratio $\Theta/T_N \sim 1.6$ indicates a slight suppression of the long-range order that can be caused by a weak frustration or reduced dimensionality of the spin lattice. Our microscopic analysis (Sec. IV) reveals the latter as the main cause. The entropy $S(T_N)$ released at T_N corroborates the slight suppression of the long-range order. Indeed, by extrapolating $C_p(T)$ to $T \to 0$ and integrating C_p/T, we find $S(T_N) \simeq 5.0$ J mol^{-1} K^{-1}, which is only 43% of the total magnetic entropy $R \ln 4$ expected for $S = \frac{1}{2}$.

Below T_N, the specific heat deviates from the T^3 behavior, which would be expected in an isotropic antiferromagnet. The data below 3 K follow the activated behavior, $C_p \sim e^{-\Delta/T}$, with the magnon gap $\Delta \simeq 7$ K (Fig. 5, inset). This exponential behavior of $C_p(T)$ indicates deviations from the simple Heisenberg model and a sizable magnetic anisotropy in MoP_3SiO_{11}.

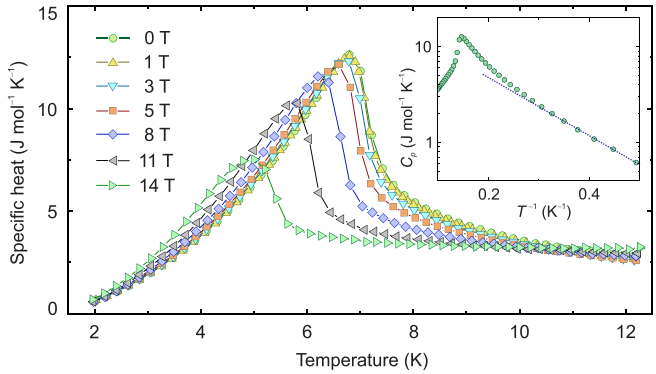

FIG. 5. Specific heat (C_p) of MoP_3SiO_{11} measured in magnetic fields up to 14 T. The inset shows activated behavior of the zero-field specific heat, with the dotted line used to determine the magnon gap $\Delta \simeq 7$ K.

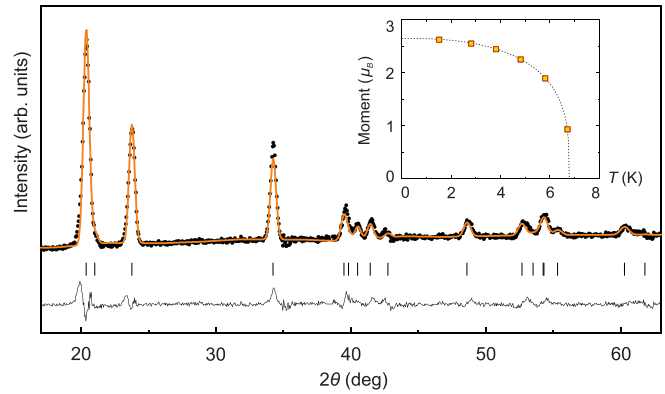

FIG. 6. Rietveld refinement for the magnetic neutron scattering obtained by subtracting the 12 K data (above T_N) from the 1.5 K data (below T_N). The orange line is the fit with the covalent magnetic form factor displayed in Fig. 7. The inset shows temperature dependence of the ordered magnetic moment and its empirical fit explained in the text. The error bars are smaller than the symbol size.

Specific heat measurements also reveal a gradual suppression of T_N upon applying magnetic field (Fig. 5). The resulting monotonic phase boundary in the T-H phase diagram (Fig. 4, inset) distinguishes MoP_3SiO_{11} from the low-dimensional spin-1/2 antiferromagnets where T_N first increases in low fields and then gets suppressed upon increasing the field further [52–55]. Such a nonmonotonic behavior is rooted in the competition between quantum fluctuations of a Heisenberg antiferromagnet and uniaxial anisotropy introduced by the magnetic field [56]. The monotonic phase boundary observed in MoP_3SiO_{11} excludes this scenario and suggests the presence of magnetic anisotropy already in zero field.

C. Magnetic structure

Neutron diffraction data give further insight into the magnetic transition in MoP_3SiO_{11}. No additional magnetic reflections were observed below T_N, but several low-angle reflections became more intense, suggesting $\mathbf{k} = 0$ as the propagation vector. Symmetry analysis based on the $R\bar{3}c$ space group returns four irreps that are compatible with the fully compensated antiferromagnetic order, three of them are one-dimensional with the spins along c, whereas the fourth one is more complex and features spins in the ab plane of the structure. Only this irrep led to a successful refinement (Fig. 6). It comprises four basis vectors listed in Table II. The magnetic structure is fully described by BV_3 that represents collinear spins pinned to the [120] crystallographic

TABLE II. Basis vectors of the irrep ($R\bar{3}c$, $\mathbf{k} = 0$) that allows a fully compensated antiferromagnetic order with spins in the ab plane.

Mo atom	BV_1	BV_2	BV_3	BV_4
(x, y, z)	1 0 0	0 1 0	0.5 1 0	$\bar{1}$ $\overline{0.5}$ 0
$(x-y, \bar{y}, \bar{z}+\frac{1}{2})$	$\bar{1}$ 0 0	1 1 0	$\overline{0.5}$ $\bar{1}$ 0	$\overline{0.5}$ 0.5 0
$(\bar{x}, \bar{y}, \bar{z})$	$\bar{1}$ 0 0	0 $\bar{1}$ 0	$\overline{0.5}$ $\bar{1}$ 0	1 0.5 0
$(-x+y, y, z+\frac{1}{2})$	1 0 0	$\bar{1}$ $\bar{1}$ 0	0.5 1 0	0.5 $\overline{0.5}$ 0

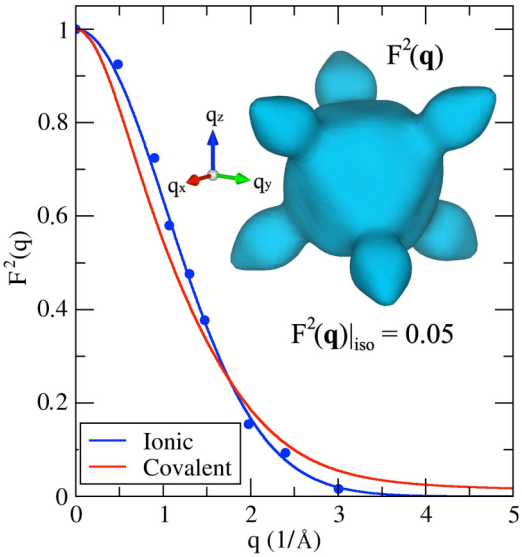

FIG. 7. Powder-averaged momentum dependence of the magnetic form factor, $|F(q)|^2$, for Mo^{3+}. The standard parametrization [57] of $F(q)$ is given by $A = 0.130$, $a = 295.027$, $B = 0.150$, $b = 2.140$, $C = 0.698$, $c = 37.935$, and $D = 0.022$ for the covalent form factor obtained in this work, and $A = 0.505$, $a = 43.558$, $B = 0.253$, $b = 28.016$, $C = 0.243$, $c = 28.804$, and $D = -0.001$ for the ionic form factor (fit to the data from Ref. [58] shown as symbols). The inset shows the $|F(q)|^2 = 0.05$ isosurface for the covalent form factor.

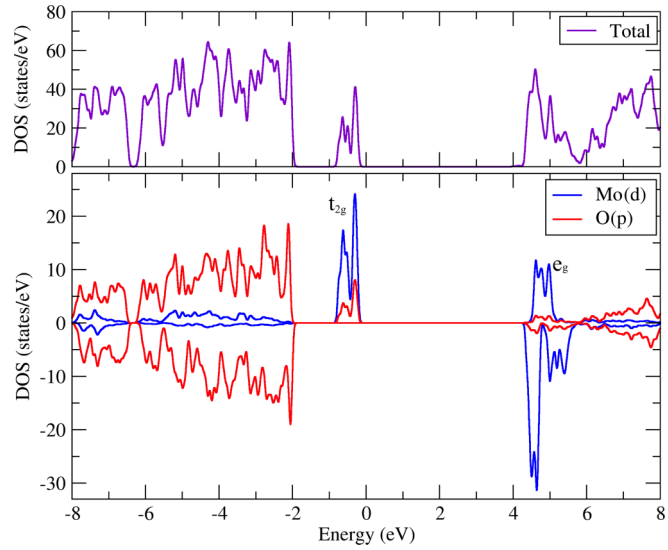

FIG. 8. (Top) GGA+U+SO total and (bottom) GGA+U partial density of states (DOS) calculated for the ferromagnetic spin configuration of MoP_3SiO_{11}. The corresponding atomic contributions are shown. The Fermi level is at zero energy.

direction (Fig. 9) or one of the equivalent directions, [210] and $[1\bar{1}0]$, obtained by a 60° rotation. The corresponding magnetic space group is $C2/c'$.

Different approximations for the magnetic form factor of Mo^{3+} were tested in the refinement. The ionic approximation was taken from Ref. [58] that reported the magnetic scattering from MoF_3. Alternatively, we compute the "covalent" form factor $F(\mathbf{q})$ by Fourier-transforming Wannier orbitals of t_{2g} symmetry, $F(\mathbf{q}) = \int |W(\mathbf{r})|^2 e^{-i\mathbf{qr}} d\mathbf{r}$ [59]. The orbitals are calculated for MoP_3SiO_{11} and thus take all peculiarities of this compound into account. The resulting nonspherical shape of $F(\mathbf{q})$ parallels the real-space arrangement of the three t_{2g} orbitals (Fig. 7). Such a custom magnetic form factor shows a somewhat different q dependence because the hybridization between the Mo $4d$ and O $2p$ orbitals (Mo–O covalency) is included. This leads to a slight improvement of the refinement. Using the 1.5 K data, we find $\mu = 2.461(8)\ \mu_B/Mo^{3+}$ and $R = 0.042$ with the ionic form factor, to be compared with $\mu = 2.634(8)\ \mu_B/Mo^{3+}$ and $R = 0.035$ when the covalent form factor is used. The 7% difference in the refined magnetic moment indicates a marginal role of covalency in MoP_3SiO_{11}, to be compared with the Mo^{4+}-containing $BaMoP_2O_8$ where the 20% difference has been reported, and a significant improvement in the quality of the refinement could be achieved [51].

The temperature dependence of the ordered magnetic moment (Fig. 6, inset) was fitted with the empirical function $\mu = \mu_0[1 - (T/T_N)^\alpha]^\beta$ that can be used across a broad temperature range and should not be confused with the critical behavior (hence neither α nor β are the true critical exponents). The fit returns $T_N = 6.78$ K, $\alpha = 2.5$, $\beta = 0.29$, and $\mu_0 = 2.65\ \mu_B$ as the zero-temperature value of the ordered magnetic moment. With $g = 1.82$ from the Curie-Weiss fit, one expects $\mu_0 = gS = 2.73\ \mu_B$. The reduction from the spin-only value of 3 μ_B is, thus, mostly caused by the spin-orbit coupling, while the reduction due to quantum fluctuations is minor.

IV. MICROSCOPIC MODELING

A. Electronic structure

The electronic density of states (DOS) for MoP_3SiO_{11} is shown in Fig. 8. One clearly identifies t_{2g} as the magnetic orbitals, whereas the e_g orbitals are empty, as expected for Mo^{3+}. The t_{2g} states in the GGA band structure are parametrized via maximally localized Wannier functions [60] using the local coordinate frame, where the axes $x'y'z'$ are directed toward oxygen atoms of the MoO_6 octahedron. The resulting Wannier functions perfectly describe the GGA bands and yield nearest-neighbor hopping parameters within the honeycomb layer (Table III).

The hopping matrices $\overleftrightarrow{t}_1$, $\overleftrightarrow{t}_2$, and $\overleftrightarrow{t}_3$ are transformed into each other by a 60° rotation about the z axis, as expected for the regular, undistorted hexagonal lattice. Additionally, we find sizable hoppings along the shortest interlayer bond with the Mo–Mo distance of 7.264 Å,

$$\overleftrightarrow{t}_c = \begin{pmatrix} -8 & -17 & 17 \\ 17 & -8 & 17 \\ 17 & 17 & -8 \end{pmatrix} \quad (1)$$

where the values are given in meV. Similar to the in-plane couplings, all three t_{2g} orbitals contribute to the hoppings. Other interlayer interactions are weak because they feature hopping matrices with a significant contribution from one orbital only. The selection of J_c as the dominant interlayer coupling is probably caused by the triple P_2O_7 bridges that are present for this coupling but absent for any other interlayer Mo–Mo contact [Fig. 1(b)]. The experimental magnetic structure (Fig. 10) reveals antiparallel spin arrangement along

TABLE III. Nearest-neighbor intralayer hopping parameters between the Mo^{3+} ions (in meV). Magnetic sites are connected by the vectors $\mathbf{r}_{t_1} = (-4.21, -2.43, -0.60)$ Å, $\mathbf{r}_{t_2} = (4.21, -2.43, -0.60)$ Å, and $\mathbf{r}_{t_3} = (0.00, 4.86, -0.60)$ Å given relative to the magnetic unit cell with the $C2/c'$ symmetry.

$\overleftrightarrow{t}_1$			$\overleftrightarrow{t}_2$			$\overleftrightarrow{t}_3$		
−16	−18	43	5	−35	−18	25	43	−35
43	−35	25	−18	43	−16	−35	−18	5
18	−5	35	35	−25	43	−43	16	18

the J_c pathway and confirms J_c as the leading interlayer coupling.

B. Exchange interactions

We will now compute relevant magnetic interactions in MoP_3SiO_{11}. To this end, we define the spin Hamiltonian

$$\hat{\mathcal{H}} = J \sum_{i>j}^{nn} \hat{\mathbf{S}}_i \hat{\mathbf{S}}_j + J_c \sum_{i>j}^{nnn} \hat{\mathbf{S}}_i \hat{\mathbf{S}}_j + D \sum_i \hat{S}_{iz}^2 \tag{2}$$

with isotropic couplings within (J) and between (J_c) the honeycomb planes. Magnetic anisotropy is introduced by the single-ion term D, which is defined relative to the three-fold axis of the crystal structure. In Sec. IV C, we show that magnetic anisotropy energy of MoP_3SiO_{11} is dominated by this term, whereas contributions of intersite terms are negligible.

The respective spin lattice is visualized in Fig. 9. In contrast to other hexagonal magnets, each lattice site features only one interlayer coupling, either to the layer above or to the layer below. This unusual coupling scheme is a corollary of the *ABCABC* stacking sequence that allows only one J_c contact per Mo^{3+} ion [Fig. 1(b)].

Exchange interactions are calculated by a mapping procedure [61] using total energies of collinear spin configurations,

$$J_{ij} = \frac{1}{4zS^2}(E_{\uparrow\uparrow} + E_{\downarrow\downarrow} - E_{\uparrow\downarrow} - E_{\downarrow\uparrow}), \tag{3}$$

where z is the number of neighbors, which have the same interaction J_{ij}. $E_{\uparrow\downarrow}$ represents the total energy of the spin state with opposite directions of the magnetic moments on the sites i and j. Total energies are calculated on the DFT+U+SO level with the Hund's coupling $J_H = 0.8$ eV and on-site Coulomb repulsion $U = 4 - 5$ eV, which is higher than the optimal $U = 3$ eV for Mo^{4+} in $BaMoP_2O_8$ [51] because the lower oxidation state of Mo in MoP_3SiO_{11} reduces covalency and screening. The double-counting correction in the atomic limit was used [62].

Exchange interactions obtained for several values of the U parameter are listed in Table IV. Both J and J_c decrease upon increasing U, as typical for the kinetic antiferromagnetic superexchange arising from the electron hoppings.

The optimal value of U is chosen on the basis of the Curie-Weiss temperature calculated as

$$\Theta = -\frac{S(S+1)}{3}(3J + J_c) \tag{4}$$

and compared to the experimental value of -10.7 ± 0.4 K that returns $U = 4.5$ eV. In the following, we take the same value of U to calculate the magnetic anisotropy of the Mo^{3+} ion.

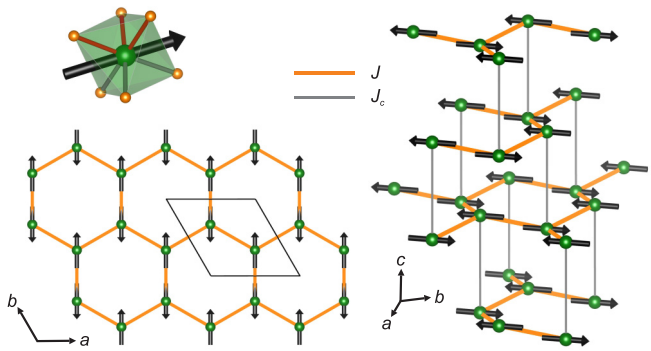

FIG. 9. Experimental magnetic structure of MoP_3SiO_{11} superimposed on the spin lattice with the in-plane coupling J and interplane coupling J_c.

C. Magnetic anisotropy

We first analyze changes in the total energy upon a uniform rotation of all spins. Using a finite number of representative spin directions [63], we extrapolate the energy dependence for an arbitrary direction over a sphere surrounding the magnetic ion [Fig. 10(a)]. The energy distribution gives a clear witness of the easy-plane anisotropy and identifies [001] as the magnetic hard axis with the respective anisotropy energy of $E_{\text{anis}} \simeq 5.0$ K. Additionally, a weak anisotropy of about 0.1 K is found in the *ab* plane beyond the anisotropy term included in Eq. (2). The lowest energy is obtained for spins directed along [120] in agreement with the magnetic moment direction determined experimentally.

In the following, we focus on the leading easy-plane anisotropy that distinguishes the *ab* plane from *c* as the magnetic hard axis. This magnetic anisotropy can arise from both single-ion and intersite terms. They are distinguished in a calculation where one spin is rotated in the plane spanned by [120] (a direction within the easy plane) and [001] (hard axis), while all neighboring spins are orthogonal to this plane. This

TABLE IV. Isotropic exchange interactions J and J_c, magnetic moment μ of the Mo^{3+} ion, and the Curie-Weiss temperature Θ depending on the on-site Coulomb repulsion parameter U within DFT+U+SO.

	$U = 4$ eV	$U = 4.5$ eV	$U = 5$ eV
J (K)	2.80	2.60	2.15
J_c (K)	0.90	0.80	0.70
μ (μ_B)	2.70	2.72	2.75
Θ (K)	−11.6	−10.8	−8.9

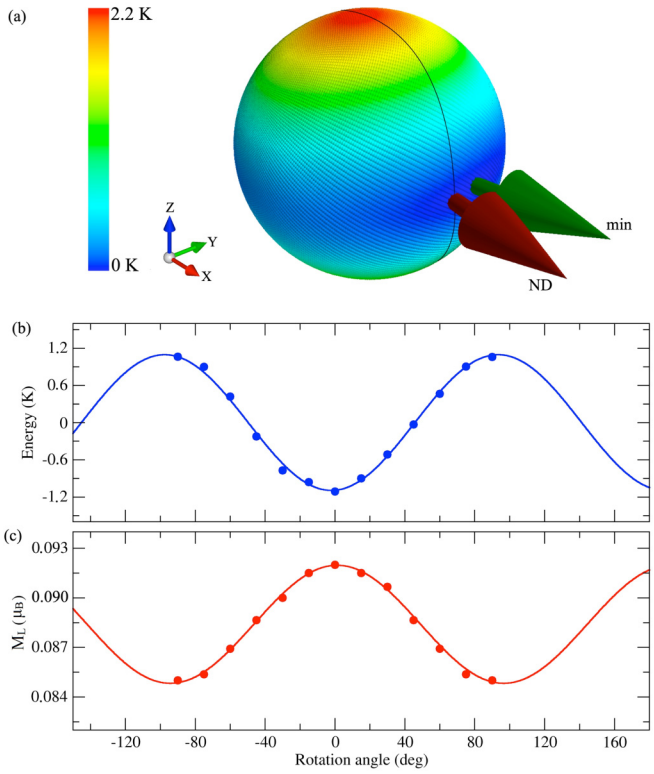

FIG. 10. (a) Magnetic anisotropy energy E_{anis}/S^2 obtained by extrapolating a finite number of spin configurations. The red arrow "ND" denotes the magnetic moment direction from the neutron diffraction experiment, whereas the green arrow "min" stands for the optimal direction in DFT+U+SO. This optimal direction is stabilized by the tiny anisotropy within the easy plane. The black line schematically represents the rotation plane for (b) and (c). (b) The dependence of E/S^2 on the rotation of a single spin in the plane spanned by [120] ($\varphi = 0°$, energy minimum) and [001] ($\varphi = 90°$, energy maximum). (c) Angular dependence of the orbital moment upon the same rotation.

procedure eliminates the contribution of intersite anisotropy and separates the single-ion term $D \simeq 2.2$ K [Fig. 10(b)]. It gives the major contribution to the anisotropy energy, $DS^2 \simeq 4.95$ K, and follows the angular dependence of the orbital moment [64,65] [Fig. 10(c)]. The highest value of the orbital moment is obtained for the direction within the easy plane. This orbital moment is antiparallel to the spin moment, thus supporting the reduction of the g value below 2.0. The total moment of 3–0.09 $\simeq 2.9$ μ_B is slightly higher than 2.73 μ_B expected from $g = 1.82$ determined experimentally.

D. Model simulations

We will now compare these microscopic results with the experimental data. We first use the simplest magnetic model of decoupled honeycomb planes ($J_c = 0$, $D = 0$) that allows a decent description of the high-field magnetization data (Fig. 4), as well as of the magnetic susceptibility data down to T_N (Fig. 3). The fitted parameters of $J = 2.6$ K and $g = 1.82$ are in an excellent agreement with the results of our *ab initio* calculations and Curie-Weiss analysis, respectively.

One aspect missing in this simplified description is the formation of the long-range magnetic order that would be forbidden at any finite temperature in the 2D Heisenberg antiferromagnet with $J_c = 0$ and $D = 0$. Either of J_c and D leads to a finite T_N that we evaluated using scaling properties of the spin stiffness [56,66] obtained from QMC. With $D = 2.2$ K ($D/J = 0.85$), one expects $T_N = 5.2$ K, which is slightly below the experimental value of 6.8 K in zero field. By the same token, the interlayer coupling $J_c = 0.8$ K alone ($J_c/J = 0.3$) would yield the underestimated value of $T_N = 5.5$ K. Using both $D/J = 0.85$ and $J_c/J = 0.3$, we arrive at $T_N = 7.1$ K in an excellent agreement with the experiment, thus completing the microscopic description of MoP_3SiO_{11}. Moreover, from the spin-wave expression for the magnon gap $\Delta = 2DS = 3D$ [67], we estimate $\Delta = 6.6$ K in a remarkable agreement with the experimental value of about 7 K (Sec. III B). Note that this gap is associated with the easy-plane anisotropy of MoP_3SiO_{11}. The additional weak anisotropy within the easy plane could not be resolved in our present experiments and requires a further dedicated study.

It is also worth noting that our experimental value of the ordered magnetic moment is only marginally reduced compared to 3 μ_B expected for spin-3/2. This reduction is mostly accounted for by the weak orbital moment inferred from $g = 1.82$. Therefore, quantum fluctuations are expected to play a minor role in the ground state. Indeed, estimating the ordered magnetic moment for the $J - J_c$ model ($D = 0$) via the standard extrapolation procedure [68,69] results in 2.72 μ_B, about 10% reduction. This can be compared to the 45% reduction in the honeycomb antiferromagnet with spin 1/2 [70]. Large single-ion anisotropy should suppress quantum fluctuations even further.

V. DISCUSSION AND SUMMARY

MoP_3SiO_{11} is a $4d^3$ honeycomb antiferromagnet with the disconnected MoO_6 octahedra. It reveals a sizable spatial anisotropy of exchange couplings ($J_c/J = 0.35$) but also a substantial single-ion magnetic anisotropy D, which is similar in magnitude to the leading exchange coupling J. This anisotropy chooses the in-plane spin direction of the collinear antiferromagnetic order established by J and J_c. It also enhances T_N and keeps the ordered magnetic moment close to its classical value. The size of the ordered moment in MoP_3SiO_{11} can be accounted for by the weak orbital contribution without invoking quantum effects. This indicates only a minor role of quantum fluctuations in the ground state of this spin-3/2 antiferromagnet.

Other $4d^3$ honeycomb antiferromagnets show a very different balance between D and J. For example, $SrRu_2O_6$ features $|D|/J = 0.028$ [24] to be compared with $D/J = 0.85$ in MoP_3SiO_{11}. This leads to a significant difference in the relative size of the magnon gap, $\Delta/J = 0.83$ in $SrRu_2O_6$ vs. $\Delta/J = 2.7$ in MoP_3SiO_{11}. Both differences can be traced back to the reduction in J for MoP_3SiO_{11} with its disconnected MoO_6 octahedra. However, also the D value changes drastically, from -14 K (easy-axis anisotropy) in $SrRu_2O_6$ to $+2.2$ K (easy-plane anisotropy) in MoP_3SiO_{11}. This change correlates with the local distortion of the transition-metal octahedra that show the compression along the threefold axis in

$SrRu_2O_6$ ($\alpha = 93.2^\circ$) versus elongation along the three-fold axis in MoP_3SiO_{11} ($\alpha = 88.8^\circ$), see Fig. 1 for the definition of the angle α. In both cases, single-ion anisotropy has a strong impact on the magnetism, despite the quenched orbital moment of the d^3 ions. Unquenching the orbital moment increases the anisotropy further. For example, one finds $|D| \simeq 70$ K in $BaMoP_2O_8$ with Mo^{4+} [71].

In summary, we revised the crystallographic symmetry of the MoP_3SiO_{11} silicophosphate and showed that its space group is $R\bar{3}c$, resulting in the formation of perfect honeycomb planes of the spin-$\frac{3}{2}$ Mo^{3+} ions. Their magnetic moments are quite robust as a result of the half-filled t_{2g} shell and Hund's coupling. Magnetic couplings within the honeycomb planes ($J \simeq 2.6$ K) are three times stronger than the interplane couplings ($J_c \simeq 0.8$ K). Collinear antiferromagnetic order caused by J and J_c is reinforced by the sizable easy-plane anisotropy $D \simeq 2.2$ K that opens the magnon gap $\Delta \simeq 7$ K. Our data suggest single-ion anisotropy as a major ingredient of $4d^3$ magnets despite their nominally quenched orbital moment. Both sign and size of this anisotropy may be controlled by local deformations of the transition-metal octahedra.

ACKNOWLEDGMENTS

We are grateful to Anton Jesche for his continuous laboratory support and essential advice on thermodynamic measurements. The beam time provided by the ILL [34] and ESRF [33] was instrumental for completing this project. We thank Andy Fitch, Catherine Dejoie, and Vera Bader for their help during the data collection at ID22. We also acknowledge support by the HLD at HZDR, member of the European Magnetic Field Laboratory (EMFL).

The work of D.I.B. was supported by the Russian Science Foundation, Grant No. 21-72-10136. The work in Augsburg was supported by the Federal Ministry for Education and Research through the Sofja Kovalevskaya Award of Alexander von Humboldt Foundation (A.A.T) and by the German Research Foundation (DFG) via the Project No. 107745057 (TRR80). L.D. acknowledges support from the Rutherford International Fellowship Programme (RIFP). This project has received funding from the European Union's Horizon 2020 research and innovation program under Marie Skłodowska-Curie Grant Agreement No. 665593 awarded to the Science and Technology Facilities Council.

[1] J. D. Reger, J. A. Riera, and A. P. Young, Monte Carlo simulations of the spin-1/2 Heisenberg antiferromagnet in two dimensions, J. Phys.: Condens. Matter **1**, 1855 (1989).

[2] Z. Weihong, J. Oitmaa, and C. J. Hamer, Second-order spin-wave results for the quantum XXZ and XY models with anisotropy, Phys. Rev. B **44**, 11869 (1991).

[3] J. G. Rau, E. K.-H. Lee, and H.-Y. Kee, Spin-orbit physics giving rise to novel phases in correlated systems: Iridates and related materials, Ann. Rev. Condens. Matter Phys. **7**, 195 (2016).

[4] M. Hermanns, I. Kimchi, and J. Knolle, Physics of the Kitaev model: Fractionalization, dynamic correlations, and material connections, Ann. Rev. Condens. Matter Phys. **9**, 17 (2018).

[5] S. M. Winter, A. A. Tsirlin, M. Daghofer, J. van den Brink, Y. Singh, P. Gegenwart, and R. Valentí, Models and materials for generalized Kitaev magnetism, J. Phys.: Condens. Matter **29**, 493002 (2017).

[6] H. Takagi, T. Takayama, G. Jackeli, G. Khaliullin, and S. E. Nagler, Concept and realization of Kitaev quantum spin liquids, Nat. Rev. Phys. **1**, 264 (2019).

[7] A. A. Tsirlin and P. Gegenwart, Kitaev magnetism through the prism of lithium iridate, Phys. Status Solidi B, 2100146 (2021).

[8] P. P. Stavropoulos, D. Pereira, and H.-Y. Kee, Microscopic Mechanism for a Higher-Spin Kitaev Model, Phys. Rev. Lett. **123**, 037203 (2019).

[9] P. S. Anisimov, F. Aust, G. Khaliullin, and M. Daghofer, Nontrivial Triplon Topology and Triplon Liquid in Kitaev-Heisenberg-Type Excitonic Magnets, Phys. Rev. Lett. **122**, 177201 (2019).

[10] J. Chaloupka and G. Khaliullin, Highly frustrated magnetism in relativistic d^4 Mott insulators: Bosonic analog of the Kitaev honeycomb model, Phys. Rev. B **100**, 224413 (2019).

[11] K. Momma and F. Izumi, *VESTA* 3 for three-dimensional visualization of crystal, volumetric and morphology data, J. Appl. Cryst. **44**, 1272 (2011).

[12] T.-C. Wei, I. Affleck, and R. Raussendorf, Affleck-Kennedy-Lieb-Tasaki State on a Honeycomb Lattice is a Universal Quantum Computational Resource, Phys. Rev. Lett. **106**, 070501 (2011).

[13] M. Koch-Janusz, D. I. Khomskii, and E. Sela, Affleck-Kennedy-Lieb-Tasaki State on a Honeycomb Lattice from t_{2g} Orbitals, Phys. Rev. Lett. **114**, 247204 (2015).

[14] D. Jakab, E. Szirmai, M. Lewenstein, and G. Szirmai, Competing valence bond and symmetry-breaking Mott states of spin-3/2 fermions on a honeycomb lattice, Phys. Rev. B **93**, 064434 (2016).

[15] C. I. Hiley, M. R. Lees, J. M. Fisher, D. Thompsett, S. Agrestini, R. I. Smith, and R. I. Walton, Ruthenium(V) oxides from low-temperature hydrothermal synthesis, Angew. Chem. Int. Ed. **53**, 4423 (2014).

[16] C. I. Hiley, D. O. Scanlon, A. A. Sokol, S. M. Woodley, A. M. Ganose, S. Sangiao, J. M. De Teresa, P. Manuel, D. D. Khalyavin, M. Walker, M. R. Lees, and R. I. Walton, Antiferromagnetism at $T > 500$ K in the layered hexagonal ruthenate $SrRu_2O_6$, Phys. Rev. B **92**, 104413 (2015).

[17] W. Tian, C. Svoboda, M. Ochi, M. Matsuda, H. B. Cao, J.-G. Cheng, B. C. Sales, D. G. Mandrus, R. Arita, N. Trivedi, and J.-Q. Yan, High antiferromagnetic transition temperature of the honeycomb compound $SrRu_2O_6$, Phys. Rev. B **92**, 100404(R) (2015).

[18] S. Streltsov, I. I. Mazin, and K. Foyevtsova, Localized itinerant electrons and unique magnetic properties of $SrRu_2O_6$, Phys. Rev. B **92**, 134408 (2015).

[19] Z. V. Pchelkina, S. V. Streltsov, and I. I. Mazin, Spectroscopic signatures of molecular orbitals in transition metal oxides with a honeycomb lattice, Phys. Rev. B **94**, 205148 (2016).

[20] S. Okamoto, M. Ochi, R. Arita, J. Yan, and N. Trivedi, Localized-itinerant dichotomy and unconventional magnetism in $SrRu_2O_6$, Sci. Rep. **7**, 11742 (2017).

[21] A. Hariki, A. Hausoel, G. Sangiovanni, and J. Kuneŝ, DFT+DMFT study on soft moment magnetism and covalent bonding in $SrRu_2O_6$, Phys. Rev. B **96**, 155135 (2017).

[22] Y. S. Ponosov, E. V. Komleva, D. A. Zamyatin, R. I. Walton, and S. V. Streltsov, Raman spectroscopy of the low-dimensional antiferromagnet $SrRu_2O_6$ with large Néel temperature, Phys. Rev. B **99**, 085103 (2019).

[23] D. J. Singh, Electronic structure and the origin of the high ordering temperature in $SrRu_2O_6$, Phys. Rev. B **91**, 214420 (2015).

[24] H. Suzuki, H. Gretarsson, H. Ishikawa, K. Ueda, Z. Yang, H. Liu, H. Kim, D. Kukusta, A. Yaresko, M. Minola, J. A. Sears, S. Francoual, H.-C. Wille, J. Nuss, H. Takagi, B. J. Kim, G. Khaliullin, H. Yavas, and B. Keimer, Spin waves and spin-state transitions in a ruthenate high-temperature antiferromagnet, Nat. Mater. **18**, 563 (2019).

[25] B. E. Prasad, S. Kanungo, M. Jansen, A. C. Komarek, B. Yan, P. Manuel, and C. Felser, $AgRuO_3$, a strongly exchange-coupled honeycomb compound lacking long-range magnetic order, Chem. Eur. J. **23**, 4680 (2017).

[26] W. Schnelle, B. E. Prasad, C. Felser, M. Jansen, E. V. Komleva, S. V. Streltsov, I. I. Mazin, D. Khalyavin, P. Manuel, S. Pal, D. V. S. Muthu, A. K. Sood, E. S. Klyushina, B. Lake, J.-C. Orain, and H. Luetkens, Magnetic and electronic ordering phenomena in the Ru_2O_6-layer honeycomb lattice compound $AgRuO_3$, Phys. Rev. B **103**, 214413 (2021).

[27] C. Xu, J. Feng, H. Xiang, and L. Bellaiche, Interplay between Kitaev interaction and single ion anisotropy in ferromagnetic CrI_3 and $CrGeTe_3$ monolayers, npj Quant. Mater. **4**, 57 (2018).

[28] C. Xu, J. Feng, M. Kawamura, Y. Yamaji, Y. Nahas, S. Prokhorenko, Y. Qi, H. Xiang, and L. Bellaiche, Possible Kitaev Quantum Spin Liquid State in 2D Materials with $S = 3/2$, Phys. Rev. Lett. **124**, 087205 (2020).

[29] I. Lee, F. G. Utermohlen, D. Weber, K. Hwang, C. Zhang, J. van Tol, J. E. Goldberger, N. Trivedi, and P. C. Hammel, Fundamental Spin Interactions Underlying the Magnetic Anisotropy in the Kitaev Ferromagnet CrI_3, Phys. Rev. Lett. **124**, 017201 (2020).

[30] L. Chen, J.-H. Chung, T. Chen, C. Duan, A. Schneidewind, I. Radelytskyi, D. J. Voneshen, R. A. Ewings, M. B. Stone, A. I. Kolesnikov, B. Winn, S. Chi, R. A. Mole, D. H. Yu, B. Gao, and P. Dai, Magnetic anisotropy in ferromagnetic CrI_3, Phys. Rev. B **101**, 134418 (2020).

[31] P. P. Stavropoulos, X. Liu, and H.-Y. Kee, Magnetic anisotropy in spin-3/2 with heavy ligand in honeycomb Mott insulators: Application to CrI_3, Phys. Rev. Res. **3**, 013216 (2021).

[32] A. Leclaire and B. Raveau, MoP_3SiO_{11}: A silicophosphate of molybdenum(III), J. Solid State Chem. **71**, 283 (1987).

[33] A. A. Tsirlin, V. Bader, and A. Fitch, High-resolution x-ray diffraction on the honeycomb antiferromagnet MoP_3SiO_{11}, Eur. Synchrot. Radiat. Facil. (2021), doi: 10.15151/ESRF-DC-490425598.

[34] A. A. Tsirlin, L. Ding, and C. Ritter, Magnetic structure of the $4d$ honeycomb antiferromagnet $MoSiP_3O_{11}$, Institut Laue-Langevin (2018), doi: 10.5291/ILL-DATA.5-31-2574.

[35] V. Petříček, M. Dušek, and L. Palatinus, Crystallographic computing system JANA2006: General features, Z. Krist. **229**, 345 (2014).

[36] J. Rodríguez-Carvajal, Recent advances in magnetic structure determination by neutron powder diffraction, Phys. B: Condens. Matter **192**, 55 (1993).

[37] J. P. Perdew, K. Burke, and M. Ernzerhof, Generalized Gradient Approximation Made Simple, Phys. Rev. Lett. **77**, 3865 (1996).

[38] P. Giannozzi, S. Baroni, N. Bonini, M. Calandra, R. Car, C. Cavazzoni, D. Ceresoli, G. L. Chiarotti, M. Cococcioni, I. Dabo, A. Dal Corso, S. de Gironcoli, S. Fabris, G. Fratesi, R. Gebauer, U. Gerstmann, C. Gougoussis, A. Kokalj, M. Lazzeri, L. Martin-Samos *et al.*, QUANTUM ESPRESSO: A modular and open-source software project for quantum simulations of materials, J. Phys.: Condens. Matter **21**, 395502 (2009).

[39] G. Kresse and J. Furthmüller, Efficiency of *ab-initio* total energy calculations for metals and semiconductors using a plane-wave basis set, Comput. Mater. Sci. **6**, 15 (1996).

[40] G. Kresse and J. Furthmüller, Efficient iterative schemes for *ab initio* total-energy calculations using a plane-wave basis set, Phys. Rev. B **54**, 11169 (1996).

[41] S. Todo and K. Kato, Cluster Algorithms for General-S Quantum Spin Systems, Phys. Rev. Lett. **87**, 047203 (2001).

[42] F. Alet, S. Wessel, and M. Troyer, Generalized directed loop method for quantum Monte Carlo simulations, Phys. Rev. E **71**, 036706 (2005).

[43] A. Albuquerque, F. Alet, P. Corboz, P. Dayal, A. Feiguin, S. Fuchs, L. Gamper, E. Gull, S. Gürtler, A. Honecker, R. Igarashi, M. Körner, A. Kozhevnikov, A. Läuchli, S. Manmana, M. Matsumoto, I. McCulloch, F. Michel, R. Noack, G. Pawłowski *et al.*, The ALPS project release 1.3: Open-source software for strongly correlated systems, J. Magn. Magn. Mater. **310**, 1187 (2007).

[44] H. Fukuoka, H. Imoto, and T. Saito, Synthesis and crystal structure of a new ruthenium silicophosphate: RuP_3SiO_{11}, J. Solid State Chem. **121**, 247 (1996).

[45] See Supplemental Material at http://link.aps.org/supplemental/10.1103/PhysRevB.104.094428 for crystallographic information files with the refined crystal and magnetic structures.

[46] M. A. McGuire, H. Dixit, V. R. Cooper, and B. C. Sales, Coupling of crystal structure and magnetism in the layered, ferromagnetic insulator CrI_3, Chem. Mater. **27**, 612 (2015).

[47] J. M. Rojo, J. L. Pizarro, J. Rodríguez Fernández, J. M. Greneche, M. I. Arriortua, M. T. Fernández-Díaz, and T. Rojo, Magnetic properties of $M(PO_3)_3$ (M = Fe, Mo). a comparative neutron diffraction study, J. Mater Chem. **13**, 1723 (2003).

[48] O. Janson, S. Chen, A. A. Tsirlin, S. Hoffmann, J. Sichelschmidt, Q. Huang, Z.-J. Zhang, M.-B. Tang, J.-T. Zhao, R. Kniep, and H. Rosner, Structure and magnetism of $Cr_2[BP_3O_{12}]$: Towards the quantum-classical crossover in a spin-3/2 alternating chain, Phys. Rev. B **87**, 064417 (2013).

[49] O. Janson, G. Nénert, M. Isobe, Y. Skourski, Y. Ueda, H. Rosner, and A. A. Tsirlin, Magnetic pyroxenes $LiCrGe_2O_6$ and $LiCrSi_2O_6$: Dimensionality crossover in a nonfrustrated $S = \frac{3}{2}$ Heisenberg model, Phys. Rev. B **90**, 214424 (2014).

[50] L. Lezama, J. M. Rojo, J. L. Mesa, T. Rojo, and R. Olazcuaga, Synthesis and magnetic and electrical properties of the molybdenum and tungsten pyrophosphates MP_2O_7 (M = Mo, W), J. Solid State Chem. **115**, 146 (1995).

[51] J. Hembacher, D. I. Badrtdinov, L. Ding, Z. Sobczak, C. Ritter, V. V. Mazurenko, and A. A. Tsirlin, Stripe order and magnetic anisotropy in the $S = 1$ antiferromagnet $BaMoP_2O_8$, Phys. Rev. B **98**, 094406 (2018).

[52] N. Tsyrulin, F. Xiao, A. Schneidewind, P. Link, H. M. Rønnow, J. Gavilano, C. P. Landee, M. M. Turnbull, and M. Kenzelmann, Two-dimensional square-lattice $S = 1/2$

antiferromagnet $Cu(pz)_2(ClO_4)_2$, Phys. Rev. B **81**, 134409 (2010).

[53] E. Čižmár, S. A. Zvyagin, R. Beyer, M. Uhlarz, M. Ozerov, Y. Skourski, J. L. Manson, J. A. Schlueter, and J. Wosnitza, Magnetic properties of the quasi-two-dimensional $S = 1/2$ Heisenberg antiferromagnet $[Cu(pyz)_2(HF_2)]PF_6$, Phys. Rev. B **81**, 064422 (2010).

[54] A. A. Tsirlin, R. Nath, A. M. Abakumov, Y. Furukawa, D. C. Johnston, M. Hemmida, H.-A. Krug von Nidda, A. Loidl, C. Geibel, and H. Rosner, Phase separation and frustrated square lattice magnetism of $Na_{1.5}VOPO_4F_{0.5}$, Phys. Rev. B **84**, 014429 (2011).

[55] A. A. Tsirlin, O. Janson, S. Lebernegg, and H. Rosner, Square-lattice magnetism of diaboleite $Pb_2Cu(OH)_4Cl_2$, Phys. Rev. B **87**, 064404 (2013).

[56] P. Sengupta, C. D. Batista, R. D. McDonald, S. Cox, J. Singleton, L. Huang, T. P. Papageorgiou, O. Ignatchik, T. Herrmannsdörfer, J. L. Manson, J. A. Schlueter, K. A. Funk, and J. Wosnitza, Nonmonotonic field dependence of the Néel temperature in the quasi-two-dimensional magnet $[Cu(HF_2)(pyz)_2]BF_4$, Phys. Rev. B **79**, 060409(R) (2009).

[57] P. Brown, Magnetic scattering of neutron, in *International Tables for Crystallography, Volume C: Mathematical, Physical and Chemical Tables*, edited by A. J. C. Wilson (Kluwer Academic Publishers, Dordrecht, 1995).

[58] M. K. Wilkinson, E. O. Wollan, H. R. Child, and J. W. Cable, Neutron diffraction investigation of magnetic ordering in the trifluorides of 4*d*-transition elements, Phys. Rev. **121**, 74 (1961).

[59] V. V. Mazurenko, I. V. Solovyev, and A. A. Tsirlin, Covalency effects reflected in the magnetic form factor of low-dimensional cuprates, Phys. Rev. B **92**, 245113 (2015).

[60] N. Marzari and D. Vanderbilt, Maximally localized generalized Wannier functions for composite energy bands, Phys. Rev. B **56**, 12847 (1997).

[61] H. J. Xiang, E. J. Kan, S.-H. Wei, M.-H. Whangbo, and X. G. Gong, Predicting the spin-lattice order of frustrated systems from first principles, Phys. Rev. B **84**, 224429 (2011).

[62] M. T. Czyżyk and G. A. Sawatzky, Local-density functional and on-site correlations: The electronic structure of La_2CuO_4 and $LaCuO_3$, Phys. Rev. B **49**, 14211 (1994).

[63] V. V. Mazurenko, Y. O. Kvashnin, F. Jin, H. A. De Raedt, A. I. Lichtenstein, and M. I. Katsnelson, First-principles modeling of magnetic excitations in Mn_{12}, Phys. Rev. B **89**, 214422 (2014).

[64] F. Bloch and G. Gentile, Zur Anisotropie der Magnetisierung ferromagnetischer Einkristalle, Z. Phys. **70**, 395 (1931).

[65] P. Bruno, Tight-binding approach to the orbital magnetic moment and magnetocrystalline anisotropy of transition-metal monolayers, Phys. Rev. B **39**, 865 (1989).

[66] A. A. Tsirlin, A. M. Abakumov, C. Ritter, and H. Rosner, $(CuCl)LaTa_2O_7$ and quantum phase transition in the $(CuX)LaM_2O_7$ family (X = Cl, Br; M = Nb, Ta), Phys. Rev. B **86**, 064440 (2012).

[67] E. Aguilera, R. Jaeschke-Ubiergo, N. Vidal-Silva, L. E. F. F. Torres, and A. S. Nunez, Topological magnonics in the two-dimensional van der Waals magnet CrI_3, Phys. Rev. B **102**, 024409 (2020).

[68] A. W. Sandvik, Finite-size scaling of the ground-state parameters of the two-dimensional Heisenberg model, Phys. Rev. B **56**, 11678 (1997).

[69] D. I. Badrtdinov, O. S. Volkova, A. A. Tsirlin, I. V. Solovyev, A. N. Vasiliev, and V. V. Mazurenko, Hybridization and spin-orbit coupling effects in the quasi-one-dimensional spin-$\frac{1}{2}$ magnet $Ba_3Cu_3Sc_4O_{12}$, Phys. Rev. B **94**, 054435 (2016).

[70] E. V. Castro, N. M. R. Peres, K. S. D. Beach, and A. W. Sandvik, Site dilution of quantum spins in the honeycomb lattice, Phys. Rev. B **73**, 054422 (2006).

[71] A. H. Abdeldaim, D. I. Badrtdinov, A. S. Gibbs, P. Manuel, H. C. Walker, M. D. Le, C. H. Wu, D. Wardecki, S.-G. Eriksson, Y. O. Kvashnin, A. A. Tsirlin, and G. J. Nilsen, Large easy-axis anisotropy in the one-dimensional magnet $BaMo(PO_4)_2$, Phys. Rev. B **100**, 214427 (2019).